Surface engineered angstrom thick ZnO-sheathed TiO2 nanowires as photoanodes for performance enhanced dye-sensitized solar cells — Source link ⤢

Turkan Gamze Ulusoy, Amir Ghobadi, Ali Kemal Okyay

Institutions: Bilkent University

Topics: Dye-sensitized solar cell, Passivation and Nanowire

Related papers:

- Electrochemical Photolysis of Water at a Semiconductor Electrode

- A Heterojunction Design of Single Layer Hole Tunneling ZnO Passivation Wrapping around TiO2Nanowires for Superior Photocatalytic Performance

- Optimization of 1D ZnO@TiO2 core-shell nanostructures for enhanced photoelectrochemical water splitting under solar light illumination.

- Effect of ultra-thin ZnO coating layer on the device performance of TiO2 dye sensitized solar cell

- Electrochemical properties of TiO2 encapsulated ZnO nanorod aggregates dye sensitized solar cells

PAPER

Surface engineered angstrom thick ZnO-sheathed TiO₂ nanowires as photoanodes for performance enhanced dye-sensitized solar cells†

T. G. Ulusoy,[ab] A. Ghobadi[ac] and A. K. Okyay*[abc]

This paper presents a systematic study on the effects of angstrom-thick atomic layer deposited (ALD) ZnO sheaths on hydrothermally-grown TiO₂ nanowires (NWs) used as photoanodes in dye-sensitized solar cells (DSSCs). We designed, synthesized and characterized the samples prepared using different numbers of ZnO cycles and compared their photovoltaic (PV) performances. The device consisting of TiO₂ NWs coated with the optimum thickness (two cycles) of ZnO shell exhibits a three-fold increase in efficiency compared to a control reference device. This paper reports results and features that demonstrate the passivation of surface state traps upon deposition of ZnO shells. While this passivation of surface traps provides a reduction in the back-reactions of the surface state mediated electrons (K_{ET}^{trap}), it is speculated that ZnO-induced surface band bending (SBB) substantially reduces the recombination rate of the device by reducing the recombination rate of the conduction band (CB) electrons (K_{ET}^{CB}). Moreover, an enhancement in the amount of dye uptake for ZnO-coated TiO₂ samples is observed and explained with the isoelectric point (IEP) concept. In spite of the excellent PV power conversion efficiencies achieved by the first ZnO cycles, thicker layers impede the electron injection rate, reducing the efficiency of the device by capturing the photogenerated dye electrons in ZnO quantum wells. Here, we investigate the mechanisms contributing to this unprecedented change and correlate them with the enhancement in device efficiency.

I. Introduction

With the ever-increasing demand for renewable and clean energy in recent years, dye-sensitized solar cells (DSSCs)[1] have attracted considerable attention as a viable photovoltaic (PV) technology that could compete with Si-based PVs[2] due to their ease of fabrication and low manufacturing cost.[3–7] In order to increase the light harvesting efficiency of DSSCs, new organic dyes with higher extinction coefficients and broader absorption spectra are being investigated.[8–11] In addition, approaches that yield large surface areas are utilized to further increase PV efficiency *via* higher dye loading. Colloidal crystalline nanoparticle-based TiO₂ films, which provide high surface areas, are the most widely used type of photoanodes in DSSC technology. However, their disordered state results in a low effective charge carrier mobility and a high carrier recombination rate, hindering efficient charge transport in the TiO₂ film. To improve charge transfer efficiency, one-dimensional (1D) structures such as nanotubes and nanowires (NWs) are desirable since they provide higher mobilities and lower recombination rates in addition to high surface areas.[12–14]

Moreover, hierarchical oxide nanostructures, which can provide high surface areas for dye uptake and 1D highly branched structures for better light scattering and overall light conversion efficiency, have become a hot research topic in recent years.[15,16]

Recently, the interest in optimising the interfacial layer between the dye and inorganic photoanode has grown rapidly within the DSSC community. Substantial improvement in DSSC performance could be attained by engineering the dye-TiO₂ interface in order to: (1) reduce the recombination of charge carriers by both the passivation of surface state traps at the interface and the retardation of the back-transfer of photo-injected electrons from the TiO₂ conduction band to the oxidized red-ox species; (2) increase the injection yields and collection efficiencies of photogenerated carriers from dye to TiO₂; and (3) increase the light absorption efficiency by enhancing the amount of dye uptake. Several studies show that high band-gap metal-oxide materials such as In₂O₃, ZrO₂, Al₂O₃, Nb₂O₅, Ga₂O₃ and SiO₂ could reduce recombination in DSSCs by blocking the back-transfer of electrons and thus preventing the recombination of electrons with either oxidized dye molecules or the oxidized redox couple (the latter one is thought to

UNAM – National Nanotechnology Research Center, Bilkent University, Ankara 06800, Turkey

Institute of Materials Science and Nanotechnology, Bilkent University, Ankara 06800, Turkey

Department of Electrical and Electronics Engineering, Bilkent University, Ankara 06800, Turkey. E-mail: aokyay@ee.bilkent.edu.tr

† Electronic supplementary information (ESI) available: Fig. S1–S6. See DOI: 10.1039/c4ta03445g

This journal is © The Royal Society of Chemistry 2014

J. Mater. Chem. A, 2014, 2, 16867–16876 | 16867

be particularly dominant in device performance degradation)[17–22] or reducing the density of surface trap states on the TiO_2 surface.[18,23] In addition, some studies demonstrate that metal-oxides like Nb_2O_5, $SrTiO_3$, ZrO_2 and Al_2O_3 can contribute to device performance enhancement by inducing a surface dipole at the metal-oxide/dye interface, leading to a negative shift in the TiO_2 conduction band[24] and an enhancement in the injection yield of photo-induced electrons.[25] In addition to the improved electrodynamics at the interface, improvement in device performance has also been related to dye adsorption enhancement.[22,24] Materials such as ZnO, MgO, ZrO_2 and Al_2O_3, which have high isoelectric points (IEP) compared to TiO_2, can provide more favourable host sites for carboxylic groups. This allows higher amounts of dye to be taken up on the surface of TiO_2 NWs coated with these materials compared to bare NW surfaces[26]. The increased dye loading increases the amount of light absorption. However, a serious drawback with most high band gap materials is that forward electron injection (dye to TiO_2) can be significantly impeded, and the electron injection efficiency can be totally diminished if the interfacial layer is only a couple of nanometers thick. To tackle this problem, researchers have recently shown that the electron transfer rate can be systematically tailored using ultrathin tunnelling layers prepared by a variety of coating methods. One of these methods, dip-coating, has been commonly utilized to coat electrodes.[27,28] However, this technique typically results in non-uniform thicknesses as well as the presence of pinholes on the surface, which creates unwanted conduits for electron back transfer.[29] In contrast, atomic layer deposition (ALD) is a self-limiting growth process that offers uniform and conformal coating of non-line-of-sight surfaces including high aspect ratio features (*e.g.*, dense micrometre-long NWs, as in our case). Although ALD is less cost effective compared to other deposition techniques, it ensures the uniform and conformal coating of a pinhole-free, angstrom-thick metal-oxide layer over the entire substrate surface, which is imperative to improve material/device performance, especially in high aspect ratio features.[15,16,19,21] Taking all these factors into consideration, this work aims to improve DSSC device performance through the surface modification of hydrothermally-grown TiO_2 NWs using sub-nanometer ALD-coated ZnO shell-like interfacial layers. The results show that a composite photoanode formed by an optimally thick ZnO shell wrapped around TiO_2 NWs significantly enhances the PV performance of the DSSC device by reducing surface trap states on TiO_2 NWs and increasing the dye loading amount without hampering electron injection efficiency, which is the main trade-off when using high band gap metal-oxide-coated NW-based photoanodes.

II.   Results and discussion

In order to investigate the effect of ZnO interfacial layer on the PV performance of DSSC devices, hydrothermally-grown TiO_2 photoanodes are coated with different ALD cycles of ZnO. A 3D schematic of the TiO_2–ZnO core–shell composite structure and the related dynamics of the electron transfer process are depicted in Fig. 1. The proposed DSSC device consists of four main parts: (1) a composite photoanode formed by hydrothermally-grown TiO_2 NWs on transparent conducting glass (FTO, F:SnO_2-doped, Tec 7 Ω sq^{-1}) coated with a conformal layer of sub-nanometre ZnO as a sheath; (2) *cis*-bis (isothiocyanato) bis (2,2′-bipyridyl-4,4′-dicarboxylato) ruthenium(II) (N719) as a photosensitizer; 3 an iodide/tri-iodide (I^-/I^{3-}) shuttle as an electron transfer mediator; and (4) Pt-coated conducting glass as a counter electrode.

The morphologies and structural characteristics of the composite photoanodes are investigated by scanning electron microscopy (SEM; FEI-Quanta 200 FEG) and transmission electron microscopy (TEM; FEI-Tecnai G2 F30). Fig. 1c and d show TEM and SEM images of the densely-packed TiO_2 NW arrays on the FTO substrate, respectively. Fig. 1c displays the TEM image of NWs with diameters in the range of 80–100 nm. As evidenced by the sharp selected area electron diffraction (SAED) pattern of an NW examined along the [110] zone axis and the high resolution TEM (HRTEM) image shown in the inset, the NWs are single crystalline along their entire lengths and have lattice fringes with interplanar spacings of $d_{110} = 3.25$ Å and $d_{001} = 2.9$ Å, which are consistent with the rutile phase. The [110] axis is perpendicular to the NW side walls, and the NWs grow along the [001] direction. The HRTEM image shown in Fig. 1d indicates that 10 ALD cycles result in a 1.3 nm-thick wurtzite ZnO (as confirmed in (ref. 30)) passivation layer grown conformally on single-crystalline TiO_2 NWs with a growth rate of 1.3 Å per cycle (below 10 cycles, it is difficult to discern the ZnO shell layer from the TiO_2 core). It is worth noting that the reduced growth rate on samples with a high density of NW arrays compared to planar surfaces (1.55 Å reported in (ref. 30) is attributed to the reduced diffusion of the gas precursor that results from the high aspect ratio. The SEM image also reveals (Fig. 1e) that the NWs are approximately 1.2–1.6 μm in length.

To identify the crystalline structures of the obtained samples and the orientation of the grown NWs, X-ray diffraction (XRD; PANALYTICAL, X'Pert Multi-Purpose X-ray diffractometer (MPD) instrument) analysis is performed. XRD patterns are collected over the 2θ angular range of 20–80° using Bragg–Brentano geometry (Cu Kα). The spectra (Fig. 2) clearly reveal that the diffraction peaks of the prepared TiO_2–ZnO core–shell samples are in agreement with the standard diffraction pattern of rutile TiO_2 (JCPDS, 82-0514), with the prominent (110) rutile peak. The diffraction peaks of ZnO-coated TiO_2 NWs are quite similar to those of the bare TiO_2 NWs. Moreover, no peaks associated with ZnO are observed in the XRD spectra since the shell layer is ultrathin.

High resolution X-ray photoelectron spectroscopy (XPS; Thermo, K-Alpha monochromated high-performance XPS spectrometer) measurements to monitor the formation of the TiO_2–ZnO interface and determine the surface elemental compositions provide further evidence for the existence of an angstrom-scale ZnO shell layer. XPS spectra of Ti2p and the Zn2p, which are shown in Fig. S1 (ESI†), are taken on the surface of the core–sheath design. The energy scales of the spectra are calibrated by shifting the XPS signal of the C1s peak to 284.8 eV. The spectral positions of the peaks corresponding to Ti2p$^{3/2}$ and Ti2p$^{1/2}$ are in line with literature values, and an
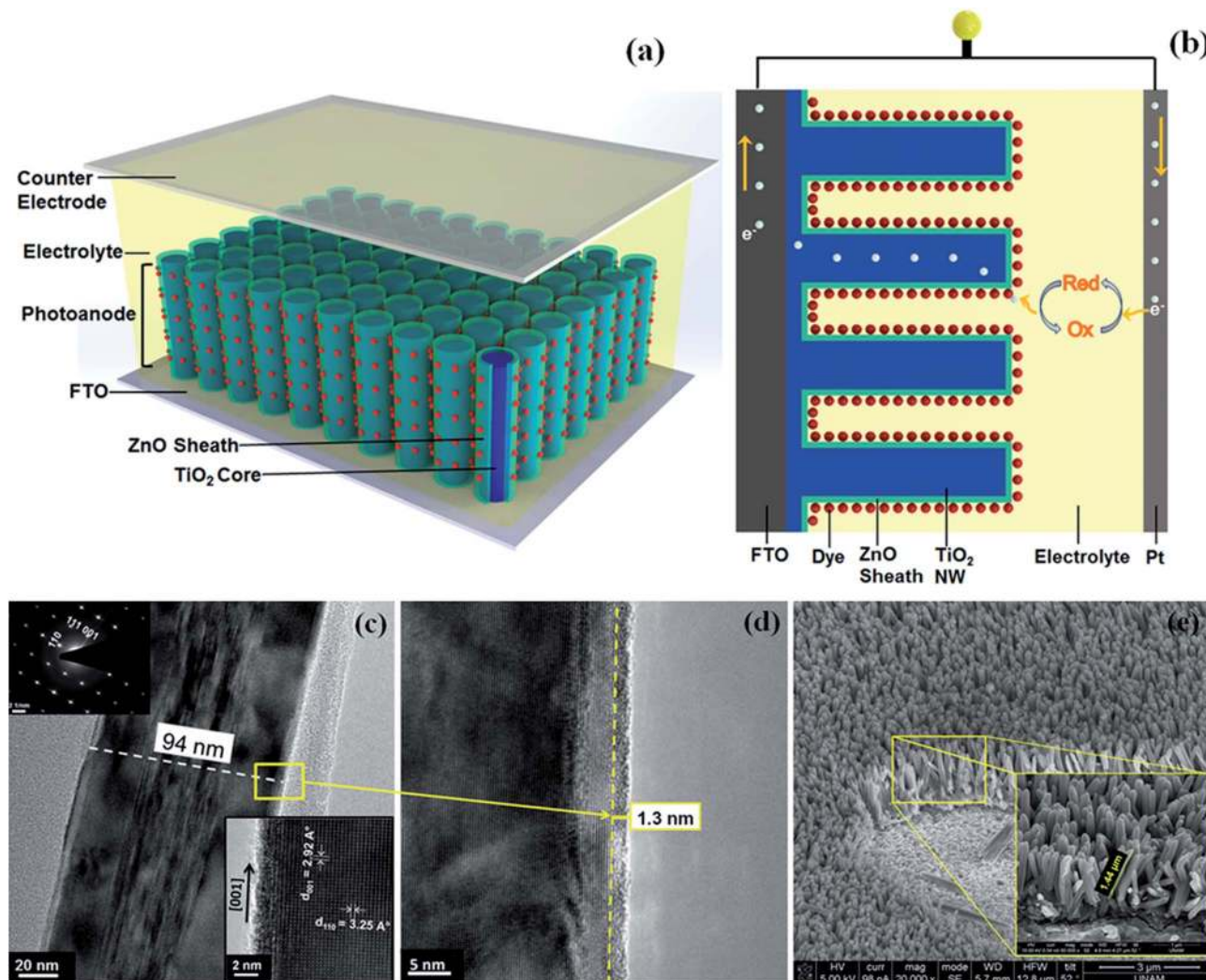
Fig. 1 Illustrative representations of (a) a 3D schematic of the TiO$_2$–ZnO core–sheath composite structure and (b) the related electronic dynamics of electron transfer in the DSSC. (c) TEM and HRTEM images of ZnO (10 ALD cycles)-coated TiO$_2$ NWs; the SAED pattern and HRTEM images in the inset prove the growth of a single crystalline rutile phase. (d) HRTEM image estimating the thickness of a ZnO sheath layer to be 1.3 nm for 10 ALD cycles. (e) SEM images (cross sectional) of densely-packed TiO$_2$ NW arrays.

expected spin orbit splitting of 5.7 eV is observed.[31,32] The 1/2 and 3/2 spin-orbit doublet components of the Zn2p spectrum and the 1045.24 eV and 1022.18 eV peak locations are also consistent with previous reports.[33] As expected, the Zn2p peak intensities, which are quite symmetric and have uniform bonding states, increase with increasing number of ALD cycles. Widening of the Ti2p is observed after four cycles, which is attributed to chemical state mixing at the TiO$_2$–ZnO interface[34] (see Fig. S1a†). As expected, the surface elemental compositions show that the ratio of Zn in the composite increases with additional ALD cycles of ZnO (Table S1†), confirming the formation of the ZnO film.

In addition, to probe surface properties of the structure, investigations on the existence of surface defects are conducted by analysing the O1s spectra of all samples. The spectrum of the core-level O1s of the TiO$_2$–ZnO core–shell can be deconvoluted into three peaks (Fig. 3a). The major peak centred at 530 eV can be assigned to the lattice oxygen bonded to Ti^{+4} ions in TiO$_2$

(L$_O$). The other two peaks with binding energies of 531.4 eV and 532.4 eV are attributed to oxygen vacancies or defects (V$_O$) and chemisorbed or dissociated oxygen species (C$_O$) on the TiO$_2$ surface.[35,36] It should be noted that the L$_O$, V$_O$ and C$_O$ peaks for the ultrathin ZnO shell layer are also located at the same binding energies;[37,38] physically adsorbed hydroxyl groups are expected to be easily removed under the ultrahigh vacuum condition of XPS system.[39] Therefore, considering that both TiO$_2$ and ZnO typically contain oxygen-related defects, it is assumed that no new Gaussian component is added for ZnO-coated samples, and all samples were fit by three independent Gaussian functions.

The results shown in Fig. 3a illustrate that for the bare TiO$_2$ sample, oxygen defect regions are present in the surface layer, but no peak is related to C$_O$ species is observed (its peak value is roughly four orders of magnitude smaller than the V$_O$-related peak). The deposition of one cycle ZnO layer on the TiO$_2$ core sharply reduces the concentration of defect states, and a small

This journal is © The Royal Society of Chemistry 2014
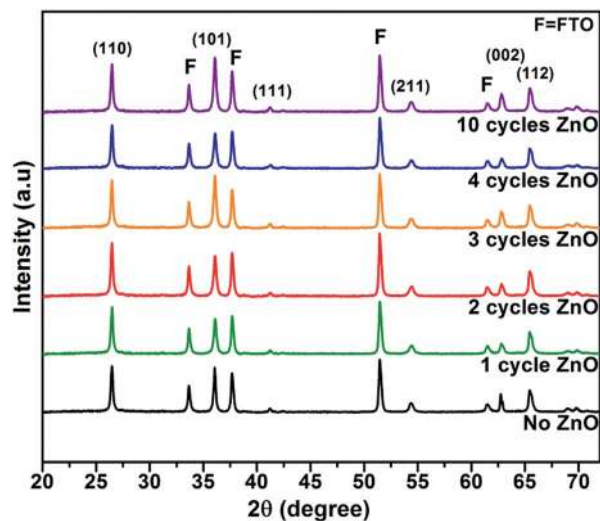
J. Mater. Chem. A, 2014, 2, 16867–16876 | 16869

Fig. 2 XRD patterns of TiO_2–ZnO core–sheath composite structures for different ALD cycles of ZnO sheath layer. Diffraction peaks are in accordance with a standard diffraction pattern of rutile structure of TiO_2 with the prominent peak for (110) direction.

shoulder at 532.4 eV is observed. This proves that the TiO_2 surface is partially coated with hydroxyl groups (*i.e.*, –OH, H_2O) that are strongly bound to the surface defects. For the thicker ZnO shell layers, the area related to V_O shows a nearly constant feature, while the concentration of C_O radicals rises almost linearly. The C_O peak becomes more significant for 10 cycles of coated sample. As previously mentioned, the ALD method is employed for the surface modification of the TiO_2 NWs. In the ALD process of ZnO, the substrate is first exposed to gaseous precursor molecules of water vapour. Based on the calculation of free energy by classical nucleation theory, most of the water-derived hydroxyl groups such as OH radicals and H_2O will be chemisorbed near imperfections such as defects (like V_O levels) and grain boundaries as well as on Ti_{5C} sites away from the vacancies at smaller concentrations.[40–43] Therefore, at oxygen vacancy positions, Ti atoms exposed at the TiO_2 surface bond to water-induced hydroxyl groups, and water-induced H ion is subsequently chemisorbed on neighbouring bridging oxygen atoms.[44,45] The schematic of these processes is shown in Fig. 3c. Consequently, the ZnO shell layer is expected to passivate (or fill) oxygen vacancy defects by adding an oxygen-containing molecule attached to the surface of TiO_2. Furthermore, the shell layer introduces new trapping sites due to adsorbed hydroxyl groups. A better qualitative comparison between different samples can be attained by determining the relative areas under each Gaussian component. In this sense, the ratio of the areas associated with the V_O and C_O peaks to the total area of the O1s spectrum is shown in Fig. 3b. The sum of these ratios is also provided in the same figure.

As can be clearly seen, the sum of the two ratios is minimized at one cycle, where the efficient passivation of V_O defect states is observed along with a sufficiently low concentration of C_O species. As the thickness of the ZnO shell layer increases, the

proportion of the sum (V_O, C_O) and C_O shows a similar increasing trend.

The PV performances of DSSC devices based on the core–sheath composite photoanodes for different ZnO ALD cycles are evaluated by a Keithley 2400 source meter equipped with a Newport 67005 solar simulator and air mass filter (AM 1.5G) under a simulated solar light irradiation with an intensity of 100 mW cm^{-2}. All related parameters including the short-circuit current (J_{sc}), the fill factor (FF), and overall conversion efficiency (η) are summarized in Table 1, and Fig. 4a shows the current density–voltage (*J–V*) characteristics of these cells. As can be clearly seen, J_{sc} increases with the number of ALD cycles and reaches a maximum of 8.826 mA cm^{-2} at two cycles. Subsequently, it decreases sharply to a relatively low value of 1.652 mA cm^{-2} at 10 cycles. On the other hand, V_{oc} monotonically increases after two cycles and reaches 0.77 V at 10 cycles, where the performance is poorest. Overall, the device based on TiO_2 NWs coated with two ALD cycles of ZnO exhibits the best conversion efficiency of 3.03% (J_{sc} = 8.826 mA cm^{-2}, FF = 0.49). This efficiency is nearly triple that of the TiO_2-only DSSC with a nominal efficiency of 1.12% (J_{sc} = 3.643 mA cm^{-2}, FF = 0.43). Noting that J_{sc} is primarily determined by the light absorption strength over the solar spectrum, the substantial increase in J_{sc} can be understood by investigating the spectral incident photon-to-current conversion efficiency (IPCE) measurement results (Fig. 4b). These results imply that for samples with sub-nanometre ZnO interfacial layers, a giant UV light absorption enhancement is observed, while the IPCE in the visible range is virtually diminished for the coated samples.[46] This quenching of IPCE at visible wavelengths, which will be discussed later, is mainly attributed to core–sheath conduction band alignment in which photogenerated electrons are captured at the ZnO layer while injecting through the interface.

To gain better insight into the electron injection capabilities of the devices, the mechanisms related to the injection of photoexcited electrons into the conduction band of the photo-anode are explored. The injection efficiencies of the devices with 0, 2 and 10 ALD cycles of ZnO shell are investigated using time-resolved single photon counting (TRSPC) as proposed by Koops *et al.*,[47] whereby the excited state emission decay of the adsorbed dye is monitored (ESI, Fig. S2†). Fig. S2† shows that ALD deposition of the interfacial ZnO layer results in the gradual delay of emission decay. The long-lived excited state of photogenerated electrons illustrates that the ZnO layer slows the injection kinetics of photoinduced electrons through the interface. Thus, this loss should be compensated by retarding the recombination kinetics of the injected electrons at the interface or suppressing the activity of surface trap states at the TiO_2 surface. In other words, an optimized ZnO overlayer thickness can enhance efficiency by providing an effective balance between injection and recombination.

Keeping previous results in mind, it should be noted that the mobilities of carriers inorganic semiconductors are very sensitive to surface traps;[48] such defect states can reduce the collection efficiency of the device by trapping injected electrons. On the other hand, based on the XPS results presented in the previous section, the ALD-deposited ZnO layer is expected to
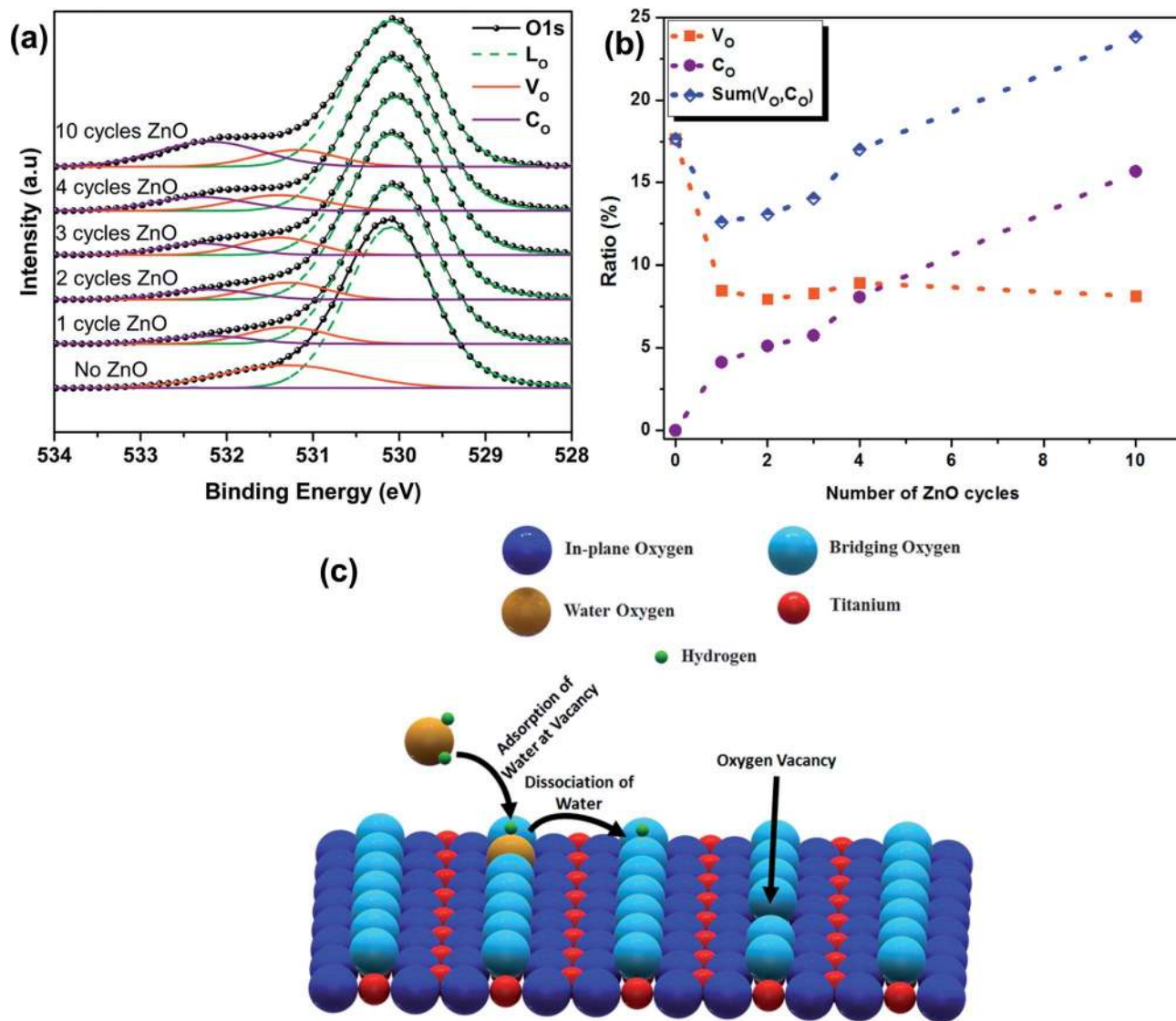
Fig. 3 (a) Core-level XPS O1s spectra of TiO_2 coated with different numbers of ALD cycles. The spectra are deconvoluted into three different peaks indicating the presence of three types of oxygen: lattice oxygen (L_O), oxygen vacancy (V_O) and chemisorbed oxygen (C_O). (b) The ratio of the areas associated with V_O and C_O peaks to the total area of O1s; the concentration of V_O defect states stays almost constant after one cycle of ZnO deposition, while C_O follows an upward trend. (c) Depiction of the mechanisms associated with water adsorption and dissociation.

Table 1 $J–V$ parameters for the experimental devices with different numbers of ZnO ALD cycles under AM 1.5G filtered spectral illumination at an incident intensity of 100 mW cm^{-2} ^{a}

# of ZnO ALD cycles	V_{oc} (V)	J_{sc} (mA cm^{-2})	FF	η (%)
0	0.71	3.643	0.43	1.12
1	0.70	5.500	0.49	1.90
2	0.70	8.826	0.49	3.03
3	0.73	6.333	0.44	2.04
4	0.75	5.367	0.36	1.43
10	0.77	1.652	0.31	0.40

^{a} Reference = 0 cycles. Values given are mean values of 4 cells prepared in a similar way. Experimental errors of the mean values are within ±10 mV for V_{oc}, ±0.20 mA cm^{-2} for J_{sc} and ±0.5% for FF.

passivate surface defects on TiO_2 NWs, reducing electron–hole (e–h) recombination during charge carrier transport to the electrodes.[49] To further evaluate the passivation effectiveness of the ultrathin ZnO sheath, photoluminescence (PL) measurements of the TiO_2–ZnO core–shell photoanodes are carried out at room temperature using an excitation wavelength of 320 nm. Consistent with XPS results, the PL spectra for all samples show a near band-edge emission (NBE) at 408 nm arising from e–h recombination across the conduction band (CB) and valance band (VB) of TiO_2, while a smaller peak associated with shallow surface defect traps emission (STE) is centred at 424 nm (Fig. 5). The peak positions are also consistent with previous reports.[50] These surface defects are well known to be due primarily to oxygen vacancies and Ti interstitials. The O1s spectra for all samples show small peaks indicating the existence of oxygen vacancies in which this V_O energy levels form a shallow donor
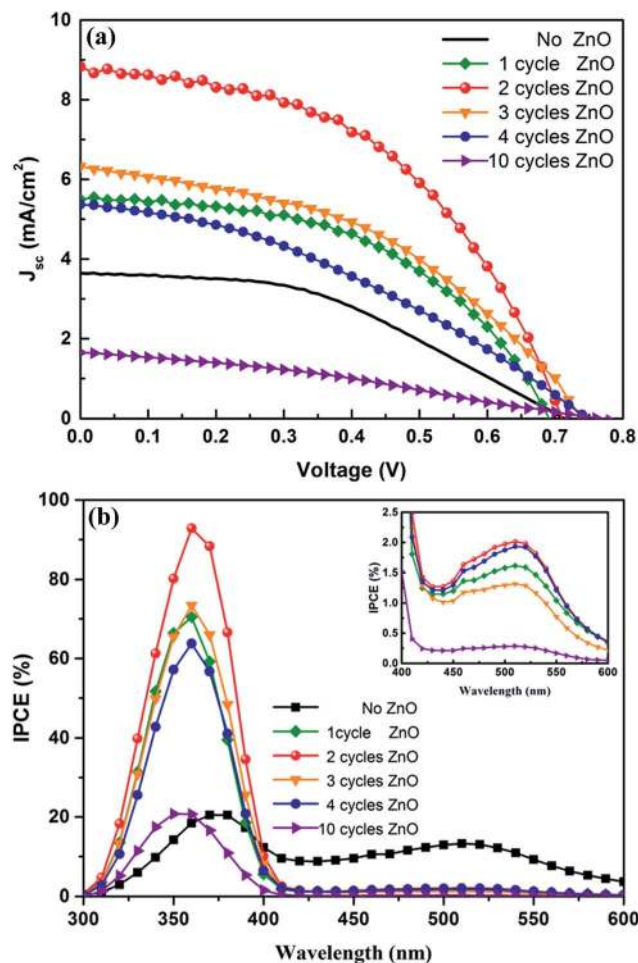
Fig. 4 The dependence of PV parameters on the number of ZnO deposition cycles on TiO_2 NWs in DSSC devices. (a) J–V curves and (b) the IPCE for the DSSCs consisting of bare TiO_2 and ZnO-coated TiO_2 core–shell composite photoanodes. The inset shows a magnified image of the IPCE for wavelengths in the range of 400–600 nm.

Fig. 5 The PL spectra for TiO_2 NWs samples coated with different numbers of ZnO cycles for an excitation wavelength of 320 nm. All samples show a near band-edge emission (NBE) at 408 nm arising from e–h recombination across the conduction band (CB) and valance band (VB) of TiO_2 and a shallow surface defect trap emission (STE) centred at 424 nm. The inset shows the ratio of STE/NBE.

state below the CB of TiO_2.[51] With this in mind, other possible surface defects can be related to Ti interstitials, which are fully ascribed to oxygen vacancies. In an ionic scheme, this is likely due to the fact that two excess electrons per V_O can be transformed to the nearest neighbouring Ti atoms, redistributing excess charges.[52] However, no trace associated with Ti interstitials is observed in our Ti2P spectra. Therefore, the dominant surface traps in our samples are attributed to V_O trap states. Revisiting the PL results, the NWs coated with two ALD ZnO cycles exhibit an intensified NBE peak compared to unpassivated sample. The deposition of one cycle of interfacial ZnO strengthens this peak through the passivation of TiO_2 surface traps (Fig. 5), but a further increase in shell thickness reduces PL intensity. A possible explanation for this reduction with thicker ZnO shell layers is hidden in the XPS results. Although the deposition of the first ALD cycles of ZnO passivates oxygen vacancy-related surface defects, the amount of chemisorbed oxygen on the core–sheath surface follows an upward trend for subsequent cycles (Fig. 3b). Based on the Madelung potential of the highly ionic crystal, these oxygen-containing molecules will
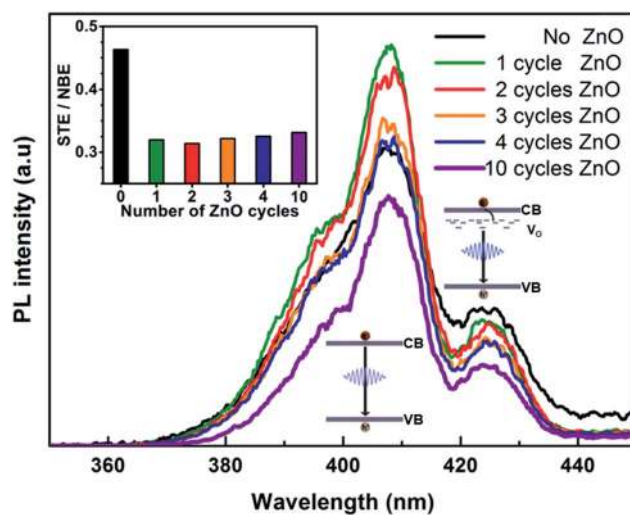
act as a new trap states in the core–shell structure.[37,44] Therefore, these chemisorbed oxygen radicals can provide an efficient charge separation that allows some of the photoexcited electrons to migrate to this localized trapping host. This separation is responsible for the reduction in NBE intensity because it reduces the probability of e–h recombination across the band gap. On the other hand, the STEs for all passivated samples exhibit a gradual quenching effect that is more pronounced for thicker shell layers. Considering that the origin of STE is generally attributed to the intrinsic V_O surface defects of TiO_2, these results strongly suggest that there is an association between the passivation of non-radiative recombination sites by ultrathin ZnO and the increment in NBE emission intensity that simultaneously quenches STE. To provide a qualitative comparison, the intensity ratio of STE/NBE is also calculated for all samples (the inset of Fig. 5). From this data, it is apparent that the ratio decreases considerably for the sample coated with one cycle of ZnO and stays almost constant for thicker layers, which is in line with the XPS measurement results.

A further understanding of the impact of the ZnO layer on the PV properties of the devices are pursued with transient photovoltage decay measurements, a useful technique to understand the charge recombination rate at the TiO_2-electrolyte interface. Fig. 6 illustrates the recombination rates extracted from these measurements for different steady-state light bias conditions. The recombination rates for all passivated samples are lower than that of the reference cell. Since the recombination rate is related to the retardation of electron back-transfer, the conduction band position of the shell layer should be several electron volts above (more negative potential) that of the TiO_2 core to effectively slow down the kinetics. However, the conduction band position of the ZnO layer is observed to be below that of the TiO_2 core. Hence, this
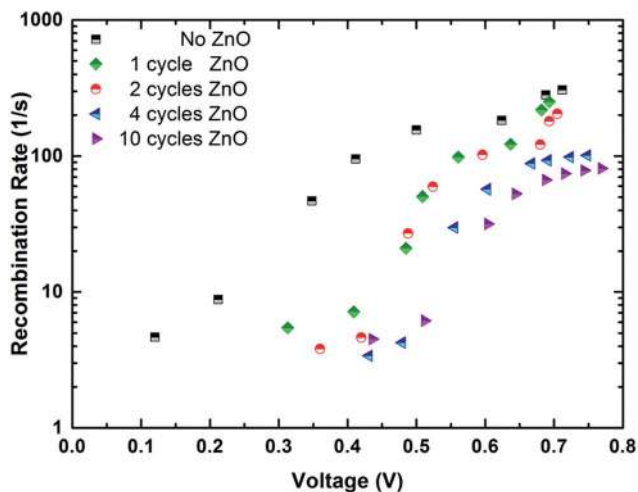
16872 | J. Mater. Chem. A, 2014, 2, 16867–16876

This journal is © The Royal Society of Chemistry 2014

Fig. 6 Electron recombination rates for different DSSC devices including bare TiO_2 NWs and TiO_2 NWs coated with different numbers of ALD ZnO cycles obtained from transient photovoltage decay measurements.

retardation of the electron back transfer rate should be attributed to ZnO-induced modification of the TiO_2 surface. According to previous studies, oxygen-containing gas molecules tend to be chemisorbed on the surface of the host material via the capture of free electrons.[36,40,41,44] As a result, these chemisorbed oxygen radicals reduce the density of free carriers in the vicinity of the surface and deplete the surface electron states.[53,54] This triggers the formation of the space charge region and band bending near the NWs surface. Looking back to the XPS results, the density of chemisorbed oxygen exhibits an increasing trend as the ZnO shell layer thickens. Thus, it is speculated that ZnO-induced surface band bending (SBB) will be more pronounced for subsequent ALD cycles. It should be noted that back-reaction of injected electrons occur mainly via two routes: (1) the direct recombination among CB; or 2) exponentially distributed trap-mediated electrons with oxidized redox couples. Therefore, the ZnO shell layer will reduce both recombination rates (K_{ET}^{CB} and K_{ET}^{trap}) by inducing an effective SBB at the TiO_2 surface and reducing surface trap density at the interface, respectively. Keeping this in mind, the ZnO layers will reduce recombination rates just due to passivation of surface traps, and the addition of more layers will generate the SBB effect in addition to the passivation effect. Consequently, a more efficient reduction in the recombination rate of injected electrons will be provided.

In addition to suppressing the recombination of photo-generated electrons across the interface, the ZnO shell layer can enhance device performance by modifying NW surfaces due to its its high isoelectric point (the IEP of ZnO is 9 compared to 5 for TiO_2 (ref. 24). The IEP defines the PH at which the oxide surface has a net zero charge.[55] The ZnO layer, as an alkali material with pH > 7, will be positively charged; hence, it will be a more favourable host site for the acidic carboxylic chains of N719 (pH <7). Therefore, dye adsorption is expected to be increased by the introduction of the ZnO layer. To substantiate this claim, dye adsorption measurements are performed using a

microplate reader (Spectramax M5) to investigate dye adsorption as a function of the number of ALD cycles. The amount of dye adsorbed on the photoanode is calculated after desorption of N719 dye from the surface using a 1 : 1 ethanol–0.1 M NaOH solution Fig. 7; details of the measurements are explained in ESI, Fig. S3–S4†). Although the first cycle of ZnO causes a small increase in dye uptake compared to the bare TiO_2, it is well-known that the monolayer usually cannot reach 100% coverage. Fig. 7 demonstrates that there is a significant enhancement in the amount of dye adsorbed at two cycles. After two cycles, the adsorption profile increases gradually, as expected.

As mentioned earlier, the ZnO passivation layer increases power conversion efficiency up to a maximum at two cycles, and it then falls back to extremely low efficiencies at 10 cycles. In order to elucidate the physical explanation for this exponential drop in device performance, it is imperative to understand the electron injection kinetics at the interface. In this way, understanding the band alignment at the heterostructure interface can provide insight into device performance. Although some papers report a band alignment where the position of conduction band of the ZnO layer is at higher energy than that of TiO_2,[56–58] some report the opposite.[59–61] Considering this fact, we first adopted high resolution XPS to explore the band alignment of the TiO_2–ZnO core–sheath structure. To understand the electron flow process and charge transfer in the structure, the valence and conduction band offsets ((ΔE_V) and (ΔE_C), respectively) are determined using the well-established analysis technique of Kraut et al.[62] In this approach, ΔE_{CL} is the energy difference between the Zn2p and Ti2p core levels (CLs) in the TiO_2–ZnO (heterojunction) sample, as it is shown in Fig. S5;† ΔE_{CL} is found to be 563.57 eV (also see eqn (1) (ref. 63). The energy difference between the CL and the valance band maximum (VBM) for rutile TiO_2 NWs, $(E_{CL} − E_{VBM})_{TiO2}$, is determined as 456.09 eV (Fig. S6†), while its value for ZnO, $(E_{CL} − E_{VBM})_{ZnO}$, is 1018.96 eV. It should be noted that the CL spectra of Zn $2p^{3/2}$ and Ti $2p^{3/2}$ show peaks located at 1021.58 eV and
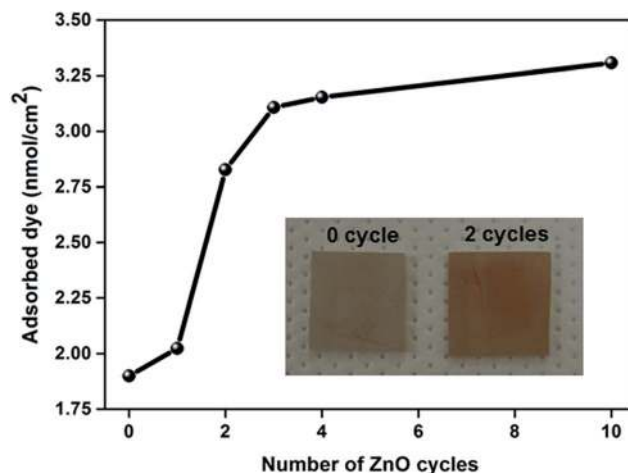

Fig. 7 The amounts of dye adsorbed on the surface of TiO_2 NWs coated with different numbers of ALD ZnO cycles, showing a sharp increase for the sample coated with two cycles. For additional cycles, the adsorbed amount follows a gradual increase.

Table 2 Results obtained from XPS valence band spectra

Sample	Region	Binding energy (eV)
TiO$_2$	Ti 2p$^{3/2}$	458.68
	VBM	2.59
ZnO	Zn 2p$^{3/2}$	1021.58
	VBM	2.62
TiO$_2$/ZnO	Zn 2p$^{3/2}$	1022.18
	Ti 2p$^{3/2}$	458.61

458.68 eV, respectively. In this regard, the calculated values of E_{VBM} are 2.62 eV for rutile TiO$_2$ (which is in good agreement with[64]) and 2.59 eV for ZnO (see Fig. S6†). All obtained data are summarized in Table 2. The optical band gap of the bare rutile TiO$_2$ NW arrays estimated from the graph of $(\alpha h\nu)^{1/2}$ *versus* $h\nu$ (Fig. S7†) is 3.02 eV.[65] The band gap of ZnO is taken as 3.37 eV at room temperature.[66] Finally, ΔE_V and ΔE_C are calculated from eqn (2) and (3) as 0.7 eV and 0.35 eV, respectively.

$$\Delta E_{CL} = (E_{Zn} - E_{TiO_2})_{TiO_2-ZnO\ core-shell} \quad (1)$$

$$\Delta E_V \left(\frac{ZnO}{TiO_2}\right) = (E_{CL} - E_{VBM})_{bulk \atop TiO_2} - (E_{CL} - E_{VBM})_{bulk \atop ZnO} + \Delta E_{CL} \quad (2)$$

$$\Delta E_C = (E_{g_{TiO_2}} - E_{g_{ZnO}} + \Delta E_V)_{TiO_2-ZnO\ core-shell} \quad (3)$$

Based on these calculations, the predicted energy band diagram of the structure is shown in Fig. 8, in which conduction band edge of rutile TiO$_2$ is 0.35 eV above that of ZnO. This band alignment would persuade the ZnO interfacial layer to act as a quantum well to capture photogenerated dye electrons.[57]

Whether photogenerated dye electrons will be captured by the potential well or escape from it depends on the well-width and initial kinetic energy of the electrons, which is related to the incident photon energy.[67] The probability that an electron will be captured increases as the thickness of the ZnO layers increases. Hence, the amount of electrons captured in the well will be exponentially increased, and the short circuit current will show a significant reduction. On the other hand, it is more likely that photogenerated electrons at lower photon energies will diffuse into the ZnO potential well towards the TiO$_2$ conduction band during thermalisation.

III. Conclusions

In conclusion, we demonstrate that by surface engineering a TiO$_2$ NWs-based photoanode using an optimized sub-nanometre-thick (2 cycles) ALD-coated ZnO interfacial sheath layer, device efficiency is boosted by about three times compared to a reference device without a ZnO shell layer. The presented results affirm that adding the angstrom-thick ZnO layer to the surface of TiO$_2$ NWs can improve cell efficiency by effectively
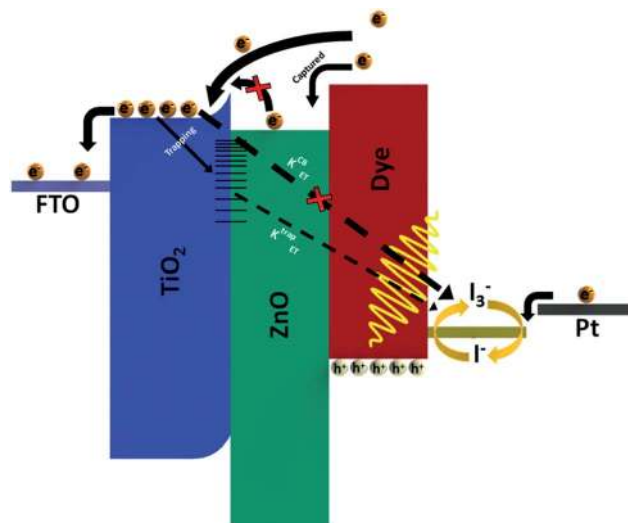

Fig. 8 Energy band diagram of a DSSC showing band alignment in the TiO$_2$–ZnO interface. Some photoexcited electrons will be captured by the ZnO well, while the rest will be injected to the CB of TiO$_2$. The ZnO passivation layer will reduce recombination rates by reducing surface trap states at the interface and inducing surface band bending at the TiO$_2$ surface.

reducing the density of surface trap states along with increasing the amount of dye uptake. As explained, although such a layer can retard the recombination kinetics for electron back-transfer at the interface, thicker layers hamper the electron injection rate. The obtained results represent a promising improvement for a wide range of applications based on TiO$_2$ NWs. These include photovoltaic and photocatalytic applications in which such an ultrathin passivation layer can reduce the recombination rate without affecting the injection kinetics and diffusion of minority carriers due to its negligible thickness.

IV. Experimental section

Ethanol, acetone, titanium butoxide (Ti(OCH$_2$CH$_2$CH$_2$CH$_3$)$_4$) (97%) and hydrochloric acid HCl (36%) are all from Sigma–Aldrich Co. and used as received. FTO-coated glass (7 Ω sq^{-1}), photosensitizer dye Ruthenizer 535-bis TBA (N719), Iodolyte HI electrolyte are all purchased from Solaronix. For ZnO deposition by ALD, diethylzinc ((C$_2$H$_5$)$_2$Zn or DEZn, Sigma-Aldrich) and HPLC-grade water (H$_2$O) are used as the zinc and oxygen precursors, respectively.

TiO$_2$ NWs are prepared on FTO glass using a hydrothermal technique. First, FTO glasses are ultrasonically cleaned for 15 min sequentially using ethanol, acetone and de-ionized (DI) water and then dried by N$_2$ flow. Concentrated HCl (20 ml) and DI water (20 ml) are mixed in a Teflon-lined stainless steel autoclave (45 ml) for 10 min, and 0.8 ml titanium butoxide is subsequently added. The mixture is stirred for an additional 30 min under ambient conditions. FTO is placed into solution so that the conducting side is facing up with a 45° angle against the autoclave wall. The hydrothermal reaction is performed at 140 °C for 4 h in an oven. Prior to removal, the FTO glass is

16874 | *J. Mater. Chem. A*, 2014, **2**, 16867–16876

This journal is © The Royal Society of Chemistry 2014

cooled to room temperature in air inside the autoclave. The NWs are then rinsed extensively with DI water and dried in air.

Finally NWs are coated with ZnO by ALD reactor (Cambridge Nanotech Savannah S100). The substrate temperature is kept at 250 °C during the ALD process using a DEZn at 80 °C and distilled water. The pulse and purge time for both is 0.015 s and 10 s, respectively. The deposition of ultrathin layers of ZnO on TiO_2 NW arrays was carried out using different numbers of successive cycles (1, 2, 3, 4 and 10) with an estimated growth rate of 1.3 Å per cycle. The ZnO-coated TiO_2 NWs are kept at 80 °C for 15 min before being soaked in 0.5 mmol N719 in a t-butanol/acetonitrile (1 : 1 by volume) solution for 24 h at room temperature. The samples are rinsed with acetonitrile to remove non-chemisorbed dye molecules. Drilled platinum-coated conducting glass is used as a counter electrode bonded to TiO_2 NWs by 25 μm-thick thermal sealant (Dupont). The active area of each cell is filled with electrolyte driven by capillary force through the hole. The area of the electrode is controlled using a mask with an area of 0.30 cm^2 on the hot-melt sealed film.

Acknowledgements

References

1 B. O'Regan and M. Gratzel, *Nature*, 1991, **353**, 737–739.

2 A. J. Nozik and J. Miller, *Chem. Rev.*, 2010, **110**, 6443–6445.

3 M. Grätzel, *J. Photochem. Photobiol., C*, 2003, **4**, 145–153.

4 N. Arrays, P. Chen, M. Takata, S. Uchida, H. Miura, K. Sumioka, S. M. Zakeeruddin and M. Gra, *ACS Nano*, 2008, **2**, 1113–1116.

5 J. R. Pitts and B. A. Gregg, *Langmuir*, 2000, **16**, 5626–5630.

6 S. Ito, N.-L. C. Ha, G. Rothenberger, P. Liska, P. Comte, S. M. Zakeeruddin, P. Péchy, M. K. Nazeeruddin and M. Grätzel, *Chem. Commun.*, 2006, 4004–4006.

7 Q. Zhang and G. Cao, *Nano Today*, 2011, **6**, 91–109.

8 N. Robertson, *Angew. Chem., Int. Ed. Engl.*, 2006, **45**, 2338–2345.

9 C. Klein, M. K. Nazeeruddin, P. Liska, D. Di Censo, N. Hirata, E. Palomares, J. R. Durrant and M. Grätzel, *Inorg. Chem.*, 2005, **44**, 178–180.

10 D. Kuang, S. Ito, B. Wenger, C. Klein, J.-E. Moser, R. Humphry-Baker, S. M. Zakeeruddin and M. Grätzel, *J. Am. Chem. Soc.*, 2006, **128**, 4146–4154.

11 M. K. Nazeeruddin, P. Péchy, T. Renouard, S. M. Zakeeruddin, R. Humphry-Baker, P. Comte, P. Liska, L. Cevey, E. Costa, V. Shklover, L. Spiccia, G. B. Deacon, C. a. Bignozzi and M. Grätzel, *J. Am. Chem. Soc.*, 2001, **123**, 1613–1624.

12 S. Y. Huang, G. Schlichtho, A. J. Nozik, M. Gra and A. J. Frank, *J. Phys. Chem. B*, 1997, **5647**, 2576–2582.

13 M. Law, L. E. Greene, J. C. Johnson, R. Saykally and P. Yang, *Nat. Mater.*, 2005, **4**, 455–459.

14 J. Van De Lagemaat, N. Park and A. J. Frank, *J. Phys. Chem. B*, 2000, **104**, 2044–2052.

15 C. P. Grigoropoulos and H. J. Sung, *Nano Lett.*, 2011, **11**, 666–671.

16 S. H. Ko, *Smart Science*, 2014, **2**, 54–62.

17 M. J. Katz, M. J. D. Vermeer, O. K. Farha, M. J. Pellin and J. T. Hupp, *Langmuir*, 2013, **29**, 806–814.

18 A. R. Pascoe, L. Bourgeois, N. W. Du, W. Xiang and Y. Cheng, *J. Phys. Chem. C*, 2013, **117**, 25118–25126.

19 T. P. Brennan, J. T. Tanskanen, K. E. Roelofs, J. W. F. To, W. H. Nguyen, J. R. Bakke, I. Ding, B. E. Hardin, A. Sellinger, M. D. Mcgehee and S. F. Bent, *J. Phys. Chem. C*, 2013, **117**, 24138–24149.

20 E. Palomares, J. N. Clifford, S. a. Haque, T. Lutz and J. R. Durrant, *J. Am. Chem. Soc.*, 2003, **125**, 475–482.

21 A. K. Chandiran, N. Tetreault, R. Humphry-Baker, F. Kessler, E. Baranoff, C. Yi, M. K. Nazeeruddin and M. Grätzel, *Nano Lett.*, 2012, **12**, 3941–3947.

22 A. K. Chandiran, M. K. Nazeeruddin and M. Grätzel, *Adv. Funct. Mater.*, 2014, **24**, 1615–1623.

23 T. C. Li, S. Go, F. Fabregat-santiago, J. Bisquert, P. R. Bueno, C. Prasittichai, J. T. Hupp and T. J. Marks, *J. Phys. Chem. C*, 2009, **14**, 18385–18390.

24 Y. Diamant, S. Chappel, S. G. Chen, O. Melamed and A. Zaban, *Coord. Chem. Rev.*, 2004, **248**, 1271–1276.

25 E. Barea, X. Xu, V. González-Pedro, T. Ripollés-Sanchis, F. Fabregat-Santiago and J. Bisquert, *Energy Environ. Sci.*, 2011, **4**, 3414.

26 A. Kay and M. Gra, *Chem. Mater.*, 2002, **14**, 2930–2935.

27 Z. L. Wang, *Annu. Rev. Phys. Chem.*, 2004, **55**, 159–196.

28 R. H. Baughman, A. a. Zakhidov and W. a. de Heer, *Science*, 2002, **297**, 787–792.

29 Z. W. Pan, Z. R. Dai and Z. L. Wang, *Science*, 2001, **291**, 2000–2002.

30 H. Ceylan, C. Ozgit-Akgun, T. S. Erkal, I. Donmez, R. Garifullin, A. B. Tekinay, H. Usta, N. Biyikli and M. O. Guler, *Sci. Rep.*, 2013, **3**, 2306.

31 S.-C. Li and U. Diebold, *J. Am. Chem. Soc.*, 2010, **132**, 64–66.

32 M. Andersson and O. Lars, *J. Phys. Chem. B*, 2002, **106**, 10674–10679.

33 S. Kwon, S. Bang, S. Lee, S. Jeon, W. Jeong, H. Kim, S. C. Gong, H. J. Chang, H. Park and H. Jeon, *Semicond. Sci. Technol.*, 2009, **24**, 035015.

34 A. R. G. Elipe and F. Yubero, *Handbook of Surfaces and Interfaces of Materials*, Academic Press, New York, 2001, vol. 2, ch. 4, pp. 147–194.

35 D. Chu, A. Younis and S. Li, *J. Phys. D: Appl. Phys.*, 2012, **45**, 355306.

36 F. Kayaci, S. Vempati, C. Ozgit-Akgun, I. Donmez, N. Biyikli and T. Uyar, *Nanoscale*, 2014, **6**, 5735–5745.

37 X. Zhang, J. Qin, Y. Xue, P. Yu, B. Zhang, L. Wang and R. Liu, *Sci. Rep.*, 2014, **4**, 4596.

38 X.-G. Han, H.-Z. He, Q. Kuang, X. Zhou, X.-H. Zhang, T. Xu, Z.-X. Xie and L.-S. Zheng, *J. Phys. Chem. C*, 2009, **113**, 584–589.

39 R. Wang, N. Sakai, A. Fujishima and T. Watanabe, *J. Phys. Chem. B*, 1999, **103**, 2188–2194.

40 P. Scheiber, A. Riss, M. Schmid, P. Varga and U. Diebold, *Phys. Rev. Lett.*, 2010, **105**, 216101.

41 S. Tan, Y. Ji, Y. Zhao, A. Zhao, B. Wang, J. Yang and J. G. Hou, *J. Am. Chem. Soc.*, 2011, **133**, 2002–2009.

42 N. G. Petrik and G. a. Kimmel, *Phys. Chem. Chem. Phys.*, 2014, **16**, 2338–2346.

43 C. Lun Pang, R. Lindsay and G. Thornton, *Chem. Soc. Rev.*, 2008, **37**, 2328–2353.

44 F. Liu, L. Lu, P. Xiao, H. He, L. Qiao and Y. Zhang, *Bull. Korean Chem. Soc.*, 2012, **33**, 2255–2259.

45 N. Bundaleski, a. G. Silva, U. Schröder, a. M. C. Moutinho and O. M. N. D. Teodoro, *J. Phys.: Conf. Ser.*, 2010, **257**, 012008.

46 J. Wu, G. Yue, Y. Xiao, J. Lin, M. Huang, Z. Lan, Q. Tang, Y. Huang, L. Fan, S. Yin and T. Sato, *Sci. Rep.*, 2013, **3**, 1283.

47 S. E. Koops, B. C. O'Regan, P. R. F. Barnes and J. R. Durrant, *J. Am. Chem. Soc.*, 2009, **131**, 4808–4818.

48 L. Zhao, M. Xia, Y. Liu, B. Zheng, Q. Jiang and J. Lian, *Materials Transactions*, 2012, **53**, 463–468.

49 Z. W. Ai, Y. Wu, H. Wu, T. Wang, C. Chen, Y. Xu and C. Liu, *Nanoscale Res. Lett.*, 2013, **8**, 105.

50 S. Mathew, A. K. Prasad, T. Benoy, P. P. Rakesh, M. Hari, T. M. Libish, P. Radhakrishnan, V. P. N. Nampoori and C. P. G. Vallabhan, *J. Fluoresc.*, 2012, **22**, 1563–1569.

51 M. K. Nowotny, L. R. Sheppard, T. Bak and J. Nowotny, *J. Phys. Chem. C*, 2008, **112**, 5275–5300.

52 G. Liu, F. Li, D.-W. Wang, D.-M. Tang, C. Liu, X. Ma, G. Q. Lu and H.-M. Cheng, *Nanotechnology*, 2008, **19**, 025606.

53 T. T. Pham, K. Y. Lee, J.-H. Lee, K.-H. Kim, K.-S. Shin, M. K. Gupta, B. Kumar and S.-W. Kim, *Energy Environ. Sci.*, 2013, **6**, 841.

54 C.-Y. Chen, J. R. D. Retamal, I.-W. Wu, D.-H. Lien, M.-W. Chen, Y. Ding, Y.-L. Chueh, C.-I. Wu and J.-H. He, *ACS Nano*, 2012, **6**, 9366–9372.

55 B. Tadesse, PhD Thesis, Brunel University, 1997.

56 K. Shen, K. Wu and D. Wang, *Mater. Res. Bull.*, 2014, **51**, 141–144.

57 S. Xuhui, C. Xinglan, T. Wanquan, W. Dong and L. Kefei, *AIP Adv.*, 2014, **4**, 031304.

58 C. Cheng, A. Amini, C. Zhu, Z. Xu, H. Song and N. Wang, *Sci. Rep.*, 2014, **4**, 4181.

59 M. Law, L. E. Greene, A. Radenovic, T. Kuykendall, J. Liphardt and P. Yang, *J. Phys. Chem. B*, 2006, **110**, 22652–22663.

60 R. A. Rakkesh and S. Balakumar, *J. Nanosci. Nanotechnol.*, 2013, **13**, 370–376.

61 Y. Xu and M. A. A. Schoonen, *Am. Mineral.*, 2000, **85**, 543–556.

62 E. A. Kraut, R. W. Grant, J. R. Waldrop and S. P. Kowalczyk, *Phys. Rev. B*, 1983, **28**, 1965–1977.

63 R. Deng, B. Yao, Y. F. Li, Y. M. Zhao, B. H. Li, C. X. Shan, Z. Z. Zhang, D. X. Zhao, J. Y. Zhang, D. Z. Shen and X. W. Fan, *Appl. Phys. Lett.*, 2009, **94**, 022108.

64 D. O. Scanlon, C. W. Dunnill, J. Buckeridge, S. a. Shevlin, A. J. Logsdail, S. M. Woodley, C. R. a. Catlow, M. J. Powell, R. G. Palgrave, I. P. Parkin, G. W. Watson, T. W. Keal, P. Sherwood, A. Walsh and A. a. Sokol, *Nat. Mater.*, 2013, **12**, 798–801.

65 F.-X. Xiao, J. Miao and B. Liu, *Mater. Horiz.*, 2014, **1**, 259.

66 L. E. Aygun, F. B. Oruc, F. B. Atar and a. K. Okyay, *IEEE Photonics J.*, 2013, **5**, 2200707–2200707.

67 A. Belsky, K. Ivanovskikh, A. Vasil'ev, M.-F. Joubert and C. Dujardin, *J. Phys. Chem. Lett.*, 2013, **4**, 3534–3538.